Chemical Physics Letters 807 (2022) 140075

Contents lists available at ScienceDirect

Chemical Physics Letters

journal homepage: www.elsevier.com/locate/cplett

Research paper

Thermal stability and fracture patterns of a recently synthesized monolayer fullerene network: A reactive molecular dynamics study

L.A. Ribeiro Junior [a,*], M.L. Pereira Junior [b], W.F. Giozza [b], R.M. Tromer [c,d], Douglas S. Galvão [c]

[a] Institute of Physics, University of Brasília, Brasília, 70910-900, Brazil
[b] Department of Electrical Engineering, Faculty of Technology, University of Brasília, Brasília, Brazil
[c] Applied Physics Department, 'Gleb Wataghin' Institute of Physics, State University of Campinas, Campinas, SP, 13083-970, Brazil
[d] Center for Computing in Engineering & Sciences, State University of Campinas, Campinas, SP, 13083-970, Brazil

HIGHLIGHTS

- qHPC60 and qTCPC60 have melting points about 3900K.
- qHPC60 and qTCPC60 have anisotropic mechanical properties.
- qHPC60 and qTCPC60 have elastic modulus of 175.9 and 100.7 GPa, respectively.

GRAPHICAL ABSTRACT

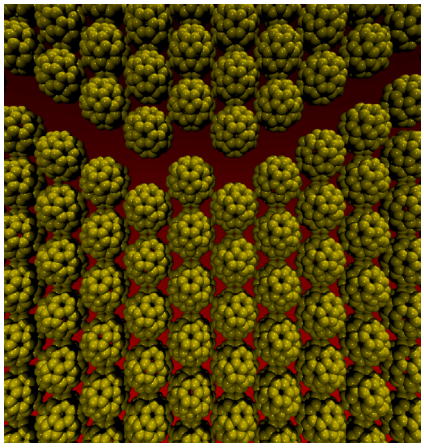

ARTICLE INFO

Keywords:
Reactive molecular dynamics
Fracture patterns
Mechanical properties
Thermal stability
2D C_{60} crystals

ABSTRACT

New monolayer 2D carbon structures, namely $qHPC_{60}$ and $qTPC_{60}$, were recently synthesized by covalently bonding C_{60} polymers. Here, we carried out Reactive (ReaxFF) molecular dynamics simulations to study the thermodynamic stability and fracture patterns of $qHPC_{60}$ and $qTPC_{60}$. Our results showed that these structures present similar thermal stability, with sublimation points of 3898K and 3965K, respectively. $qHPC_{60}$ and $qTPC_{60}$ undergo an abrupt structural transition becoming totally fractured after a critical strain threshold. The crack propagation is linear (non-linear) for $qHPC_{60}$ ($qTPC_{60}$). The estimated elastic modulus for $qHPC_{60}$ and $qTPC_{60}$ are 175.9 GPa and 100.7 GPa, respectively.

* Corresponding author.
E-mail address: ribeirojr@unb.br (L.A. Ribeiro Junior).

https://doi.org/10.1016/j.cplett.2022.140075
Received 15 August 2022; Received in revised form 21 September 2022; Accepted 22 September 2022
Available online 24 September 2022

1. Introduction

Since the discovery of graphene [1], 2D carbon materials have been widely studied to develop new optoelectronic applications [2]. Their controllable synthesis can yield different structures with distinct physical and chemical properties [3,4]. Due to this reason, the large variety of 2D carbon allotropes proposed so far [5–14] have proven to be suitable for flat electronics, although only a few structures has been experimentally realized.

Recently, new 2D carbon allotropes were synthesized: the monolayer amorphous carbon (MAC) [11] and the 2D biphenylene network (BPN) [12]. MAC is made of randomly distributed five, six, seven, and eight atom rings. BPN consists of a periodic lattice composed of fused rings containing four, six, and eight carbon atoms. Similar to graphene, MAC and BPN present a zero semi-metal bandgap, which is a serious drawback to their usage in some optoelectronic applications [15].

Very recently, 2D carbon materials with a semiconducting bandgap of about 1.6 eV – namely monolayer quasi-hexagonal-phase fullerene ($qHPC_{60}$) and monolayer quasi-tetragonal-phase fullerene ($qTPC_{60}$) – were experimentally realized overcoming the problem of a null bandgap shown by other 2D carbon-based materials [16]. It was reported that $qHPC_{60}$ and $qTPC_{60}$ show excellent environmental and thermal stabilities. The Raman spectra and optical images remain unchanged after heating, indicating that the polymeric C_{60} frameworks do not decompose up to 600 K. $qHPC_{60}$ and $qTPC_{60}$ exhibit high crystallinity and unique topological structure [16]. In this sense, a detailed description of their structural integrity with a focus on thermodynamic stability and stress resilience can pave the way for its applications.

In the present work, we investigated the thermodynamic stability and stress resilience of $qHPC_{60}$ and $qTPC_{60}$. It was observed that these materials present a well-defined (linear) elastic region when subjected to uniaxial strain. $qHPC_{60}$ and $qTPC_{60}$ undergo an abrupt structural transition to a totally fractured form after a critical strain threshold. The crack propagation is linear for $qHPC_{60}$ and non-linear for $qTPC_{60}$, respectively. Heating ramp protocol simulations revealed that they are thermally stable up to 3898 K and 3965 K, respectively.

2. Methodology

We carried out fully-atomistic MD simulations with the reactive force field ReaxFF (by employing the parameter set for C/H/O [17, 18]), as implemented in LAMMPS [19]. A reactive potential is needed (it allows the formation and breaking of chemical bonds during the dynamics) for the fracture dynamics investigation. Fig. 1 illustrates the $qHPC_{60}$ and $qTPC_{60}$ structural models (supercells) used in the MD simulations. Both structures have dimensions of 100×100 Å^2 with periodic boundary conditions and are composed of 8640 atoms. The length of the simulation box along the z-direction is 200 Å.

The equations of motion were numerically integrated using the velocity-Verlet algorithm, with a time-step of 0.2 fs. The uniaxial tensile strain was applied along the periodic x and y directions, for an engineering strain rate of 1.0×10^{-6} fs^{-1}. Before their heating and stretching, the structures were equilibrated using an NPT ensemble at a constant temperature of 300 K and null pressures using a Nosé–Hoover thermostat [20] during 200 ps.

To obtain the mechanical properties and fracture patterns, the $qHPC_{60}$ and $qTPC_{60}$ structures were continuously stretched up to their complete structural failure (fracture) by applying a maximum strain of 50%. The tensile stretching simulations were performed by increasing the x and y cell dimensions. Their thermal stability was investigated by heating up the structures from 300 K up to 10,000 K. The heating process is simulated by linearly increasing the temperature during 1 ns in an NVT ensemble. The MD snapshots and trajectories were obtained using the visualization and analysis software VMD [21].

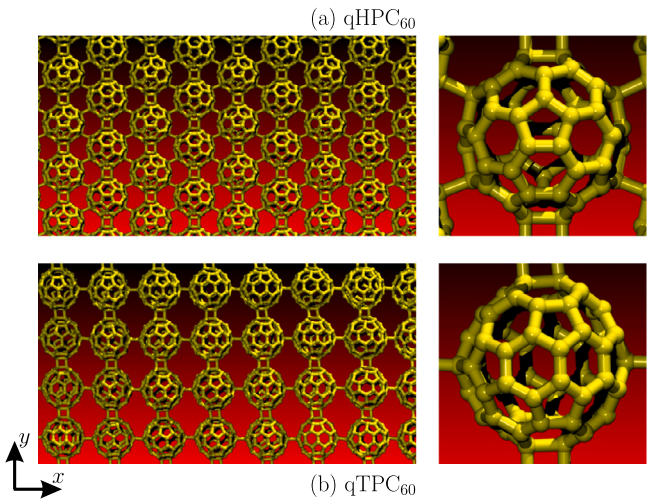

Fig. 1. Schematic representation of: (a) $qHPC_{60}$ and (b) $qTPC_{60}$ lattice structures. The right panels illustrate the corresponding unit cells.

3. Results

We begin our discussion by analyzing the $qHPC_{60}$ and $qTPC_{60}$ thermodynamic stability. The melting processes occur within the heating ramp simulations, as mentioned above. Fig. 3 illustrates the total energy (green) and heat capacity (C_V, in yellow) as a function of temperature for the melting process of $qHPC_{60}$ (Fig. 2(a)) and $qTPC_{60}$ (Fig. 2(b)). As a general trend, we can see that the total energy increases quasi-linearly with the temperature showing three different slopes: between 300 K–3500 K, 3500 K–4000 K, and 4000 K–10,000 K.

$qHPC_{60}$ and $qTPC_{60}$ maintain their structural integrity in the first stage of the heating process, defined by temperatures up to 3500 K. After this critical value, the thermal vibrations impose substantial changes in their morphologies, and the melting process occurs in the second stage of the heating process (for temperatures ranging from 3500 K up to 4500 K). The melting point is defined by the most pronounced peak in the C_V curves. In this sense, the peak in the heat capacity curve indicates the similar melting points at 3898 K (see Fig. 2(a)) and 3965 K (see Fig. 2(b)) for $qHPC_{60}$ and $qTPC_{60}$, respectively.

The third stage of the heating process (between 4000 K–10,000 K) in Figs. 2(a) and 2(b) characterizes the continuous heating of the systems. The abrupt change in the slope for the total energy curves defines a phase transition from a solid to a gas-like phase (sublimation) of the carbon atoms. The melting points obtained here for $qHPC_{60}$ and $qTPC_{60}$ are comparable to those for the monolayer graphene (4095 K) [22], MAC (3626 K) [23], and BPN (4024 K) [24].

We further explored the thermodynamic stability of $qHPC_{60}$ and $qTPC_{60}$ by analyzing the representative MD snapshots for the heating ramp simulations, with temperatures varying from 300 K up to 4000 K, as shown in Fig. 3. Figs. 2(a) and 2(e) illustrate the lattice structure for $qHPC_{60}$ and $qTPC_{60}$ at 0 K, respectively. In Figs. 2(b–c) and 2(f–g), we can note the melting process of these structures occurs differently. For the $qHPC_{60}$, the C_{60} units are fragmented into several linear atomic chains (LACs) at 1600 K, while the $qTPC_{60}$ tends to fragment into separated C_{60} units at 1200 K.

The complete atomization of the structures occurs at the related melting points, as shown in Figs. 2(d) and 2(h) for $qHPC_{60}$ and $qTPC_{60}$, respectively. Importantly, the different mechanisms observed in the melting processes are strictly related to their topology. $qHPC_{60}$ presents eight covalent bonds connecting the next-neighboring C_{60} units, whereas $qTPC_{60}$ presents only six. The higher number of covalent bonds in $qHPC_{60}$ favors the formation of LACs before the lattice atomization at 1000 K (see Fig. 2(b)). Conversely, the $qTPC_{60}$ lower

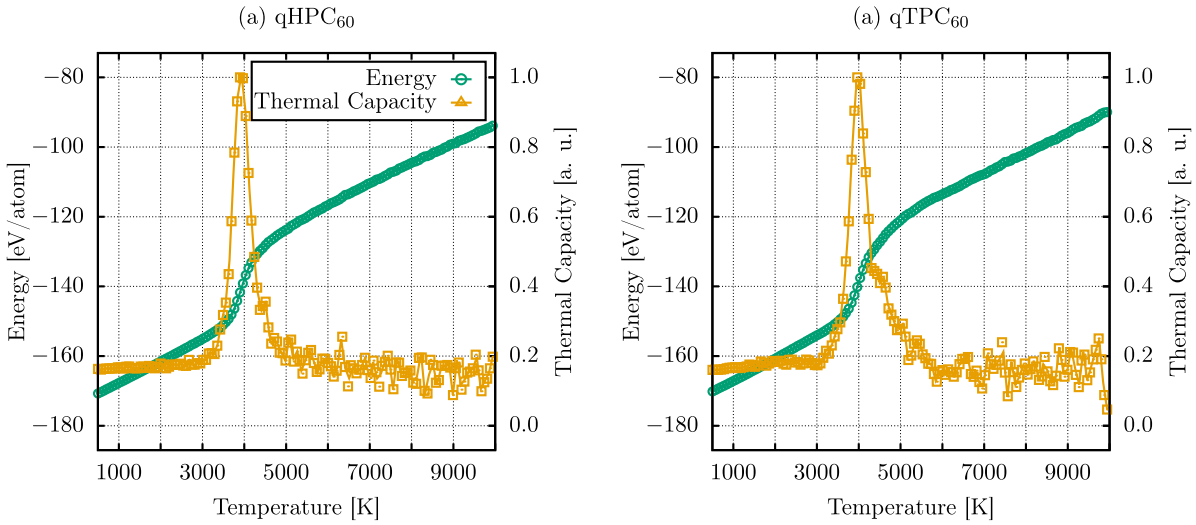

Fig. 2. Total energy and heat capacity (C_V) as a function of temperature for: (a) $qHPC_{60}$ and (b) $qTPC_{60}$ at 1 ns of the heating ramp simulations.

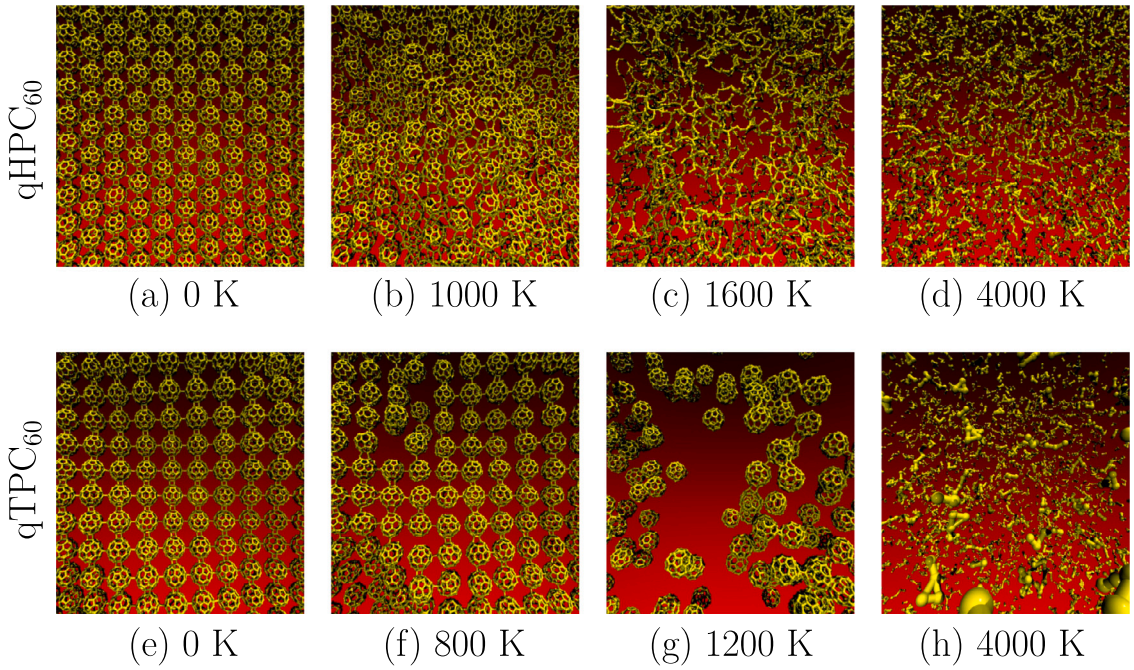

Fig. 3. Representative MD snapshots for the heating ramp simulations (melting process) for: $qHPC_{60}$ at (a) 0 K, (b) 1000 K, (c) 1600 K, and (d) 4000 K, and $qTPC_{60}$ at (e) 0 K, (f) 800 K, (g) 1200 K, and (h) 4000 K.

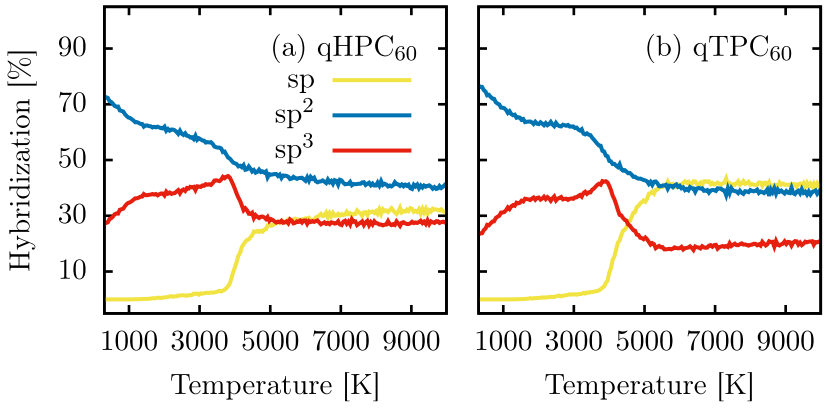

Fig. 4. Time evolution for the total number of different carbon–carbon bond types of (a) $qHPC_{60}$, and (b) $qTPC_{60}$, during their melting processes.

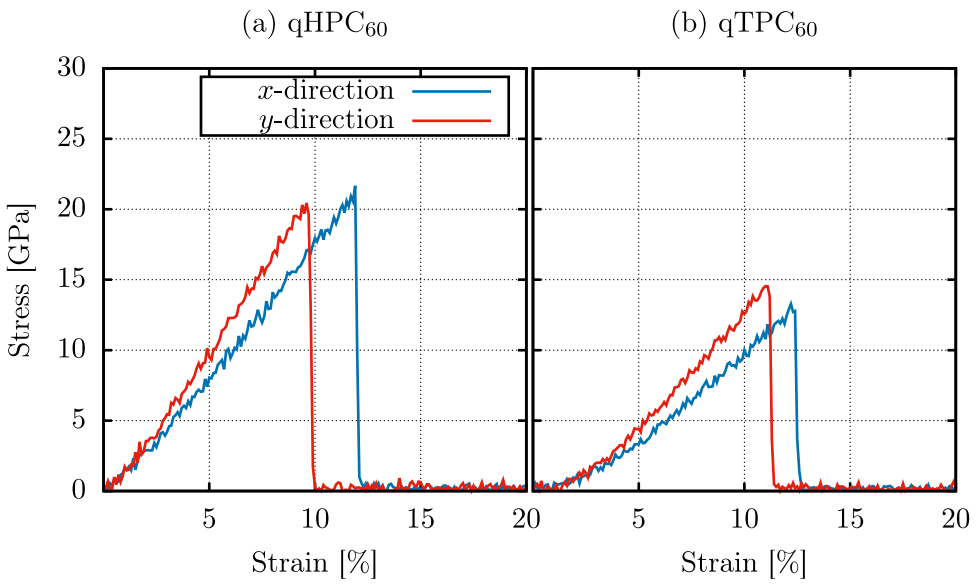

Fig. 5. Stress–strain curves for (a) $qHPC_{60}$ and (b) $qTPC_{60}$ as a function of the uniaxial applied strain in the (blue) x-direction and (red) y-direction.

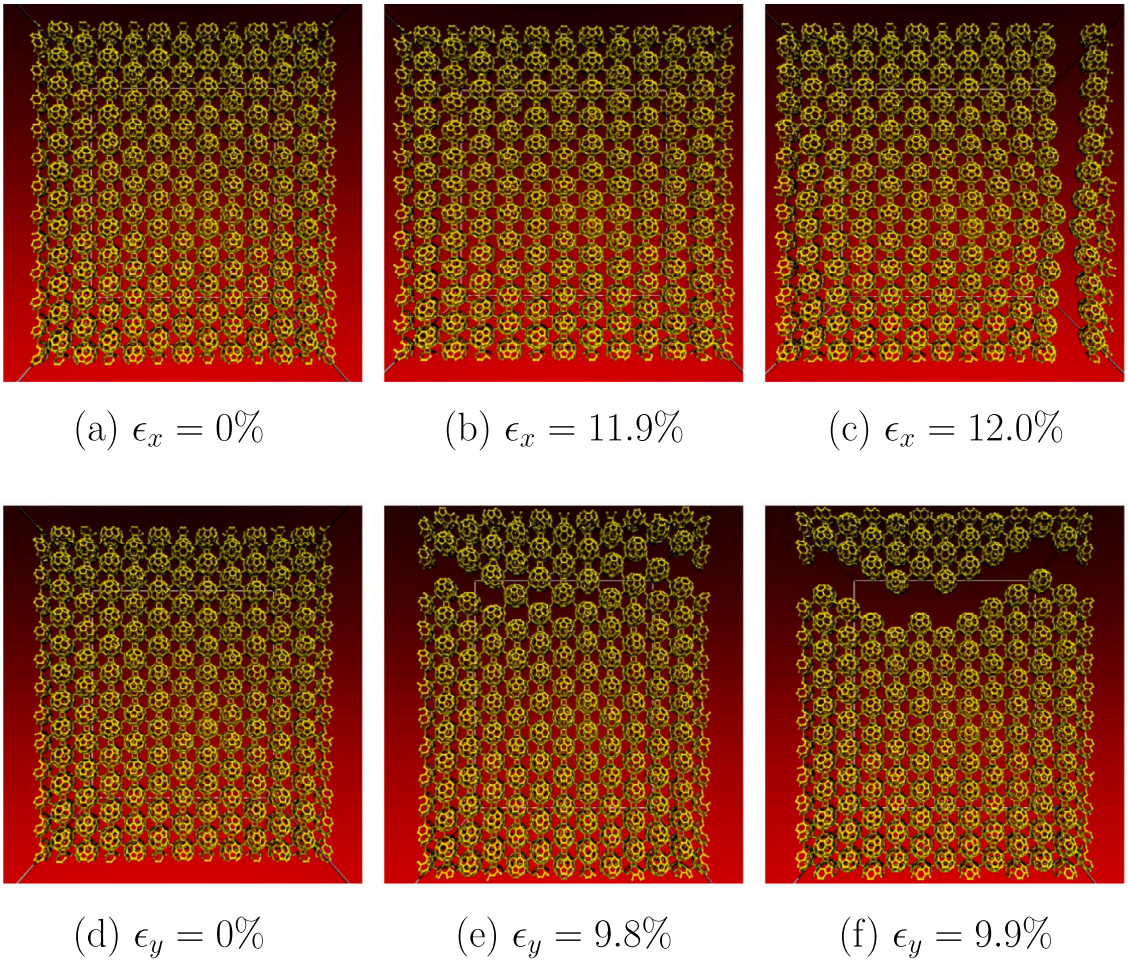

Fig. 6. Representative MD snapshots for the strain applied along the (a–c) x-direction (ε_x) and (d–f) y-direction (ε_y) for the $qHPC_{60}$ monolayer.

number of covalent bonds is responsible for its fragmentation into individual C_{60} molecules at 800 K (see Fig. 2(f)).

To gain further insights into the melting processes of $qHPC_{60}$ and $qTPC_{60}$, Fig. 4 illustrates the time evolution for the total number of different carbon–carbon bond types present in these C_60 crystals. There are two distinct stages to highlight in their melting processes: (I) the beginning of the crystal fragmentation into individual C_{60} units, which occurs at 1000 K for $qHPC_{60}$ and 800 K for $qTPC_{60}$, respectively, and

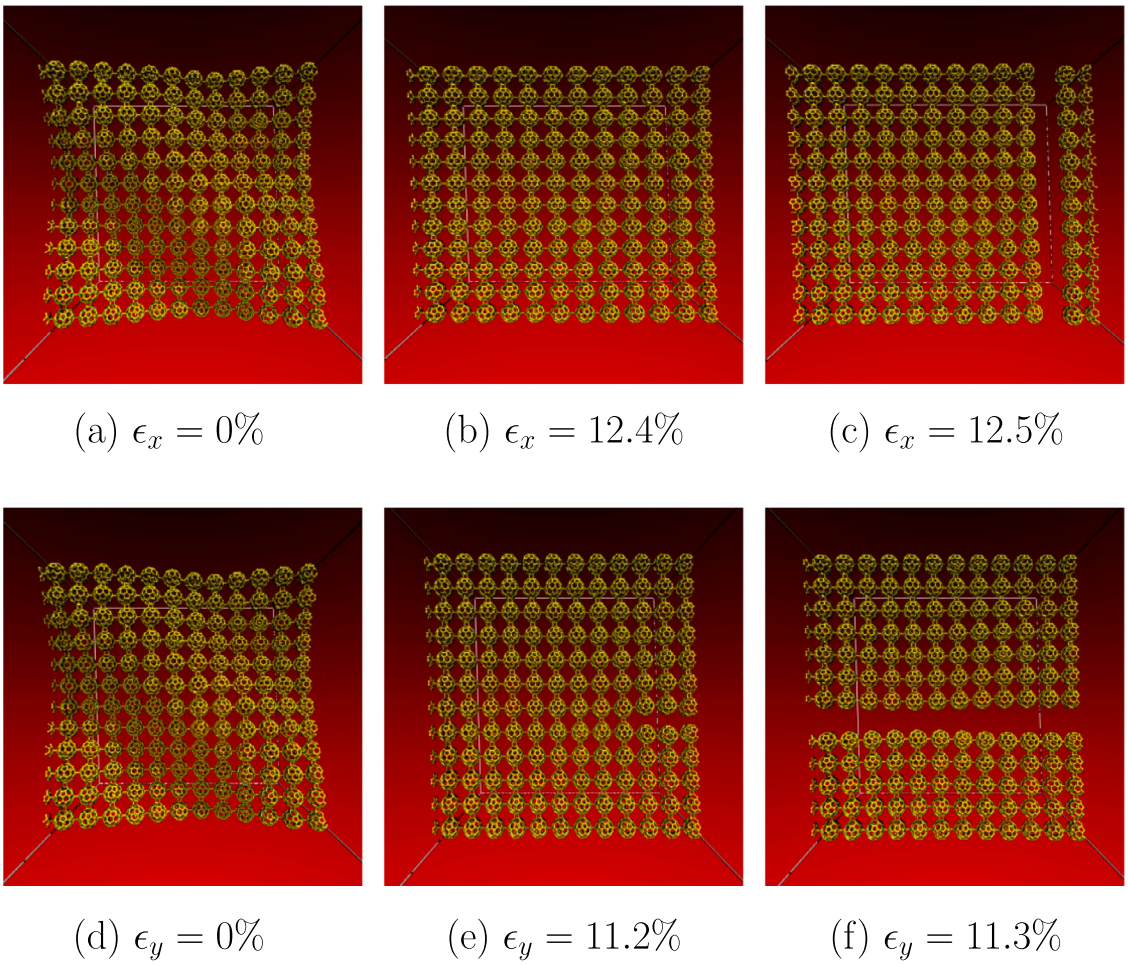

Fig. 7. Representative MD snapshots for the strain applied along the (a–c) x-direction (ε_x) and (d–f) y-direction (ε_y) for the $qTPC_{60}$ monolayer.

(II) the crystal atomization (defined as its melting point), which occurs at 3898 K for $qHPC_{60}$ and 3965 K for $qTPC_{60}$, respectively.

Figs. 4(a) and 4(b) show the total number of bonds (sp-like, sp^2-like, and sp^3-like C–C bonds) for the melting process of $qHPC_{60}$ and $qTPC_{60}$, respectively. Individual (bonded) C_{60} molecules present both sp^2- and sp^3-like C–C bonds. In the $qHPC_{60}$ and $qTPC_{60}$ lattices, sp^2-like bonds link the C_{60} units. The sp-like bonds, in turn, are present in the linear atomic chains (LACS). We can see that the initial C_{60} crystals only present sp^2- and sp^3-like C–C bonds and the hybridization percentage of sp^2-like C–C bonds is zero, as expected. At temperatures lower than the melting points, the stage (I) of the melting process, the hybridization percentage of sp^2-like C–C bonds is close to zero. This trend for the time evolution of the C–C bond types indicates that the C_{60} units remain intact.

For temperatures higher than the $qHPC_{60}$ and $qTPC_{60}$ melting points, the stage (II) of the melting process, we can observe in Figs. 4(a) and 4(b) that the hybridization percentage of sp-like C–C bonds increases abruptly to about 30% and 40%, respectively. The hybridization percentage of sp^2-like C–C bonds decreases smoothly until the end of the simulation, whereas the hybridization percentage of sp^3-like bonds increases towards the melting temperature and then decreases for higher temperatures during the LACs formation.

The stress response as a function of the uniaxial applied strain is illustrated in Fig. 5. Figs. 5(a) and 5(b) show the stress–strain curves for the uniaxial tensile loading along the x-direction (blue) and y-direction (red) for $qHPC_{60}$ and $qTPC_{60}$, respectively. The first noticeable feature is that these structures have an anisotropic mechanical behavior, which is expected because of their structural anisotropy. $qHPC_{60}$ and $qTPC_{60}$ are more resilient to tension along the x-direction than for the y-one. The presence of a ring composed of four carbon atoms linking the C_{60} units makes these structures less resilient to tension along the y-direction.

In Fig. 5, we can note that these materials present a well-defined (linear) elastic region when subjected to uniaxial strain. $qHPC_{60}$ and $qTPC_{60}$ undergo an abrupt transition from integrity to a fractured form after a critical strain of 9.6% (11.9%) along the x-direction (y-direction) and 12.2% (11.0%) along the x-direction (y-direction), respectively. The ultimate stress values for $qHPC_{60}$ and $qTPC_{60}$ are: 20.4 GPa (21.7 GPa) for the x-direction (y-direction) and 13.3 GPa (14.6 GPa) for the x-direction (y-direction), respectively. The ultimate stress is defined as the corresponding tensile stress for a critical strain. In our calculations, 1% of strain was used to estimate the following Young's modulus values for $qHPC_{60}$ and $qTPC_{60}$: 175.9 GPa (218.5 GPa) for the x-direction (y-direction) and 100.7 GPa (133.5 GPa) for the x-direction (y-direction), respectively. As mentioned above, $qHPC_{60}$ tends to be more resilient than $qTPC_{60}$ due to the higher number of covalent bonds connecting the next-neighboring C_{60} units. These values are much lower than other 2D carbon-based structures and can be explained by the high structural stability of the C_{60} units.

Finally, we discuss the fracture patterns of the $qHPC_{60}$ and $qTPC_{60}$ monolayer when subjected to uniaxial tensile loading. Figs. 6(a–c) and 6(d–f) show representative MD snapshots for the strain applied along the x-direction (ε_x) and y-direction (ε_y) for the $qHPC_{60}$ monolayer. Fig. 6(a) and 6(d) illustrate the monolayer configurations at $\varepsilon_x = 0$ and $\varepsilon_y = 0$, respectively. As can be inferred from Fig. 6(b), $qHPC_{60}$ preserves its topology as the strain increase up to $\varepsilon_x = 11.9\%$. Immediately

after this critical strain value, the lattice breaks abruptly with fast and linear crack propagation along the opposite direction of the stretch (see Fig. 6(c)).

For the $qHPC_{60}$ stretching along the y-direction, a non-linear fast crack propagation is observed along the opposite direction of the stretch at 9.8% of strain, as shown in Fig. 6(e). The total fracture of $qHPC_{60}$ is achieved at 9.9% of strain (see Fig. 6(f)). The anisotropic trend for the fracture patterns of $qHPC_{60}$ is due to the different bond arrangements that connect the next-neighboring C_{60} units along the directions of this 2D crystal. For the x-direction, four diagonal bonds connect a central unit to four neighboring units. On the other hand, along the y-direction, there are four parallel bonds linking only two neighboring units with a central one.

Figs. 7(a–c) and 7(d–f) show representative MD snapshots for the strain applied along the x-direction (ε_x) and y-direction (ε_y) for the $qTPC_{60}$ monolayer. Fig. 7(a) and 7(d) depict the monolayer configurations at $\varepsilon_x = 0$ and $\varepsilon_y = 0$, respectively. We can note that the equilibrated $qTPC_{60}$ monolayer is not planar. It preserves its topology as the strain increase up to $\varepsilon_x = 12.4\%$ (Fig. 6(b)) and to $\varepsilon_x = 11.2\%$ (see Fig. 6(e)). Immediately after these critical strain values, the lattice breaks linearly with a fast crack propagation along the opposite direction of the stretch for $\varepsilon_x = 12.5\%$ (Fig. 6(c)) and $\varepsilon_y = 11.3\%$ (Fig. 6(f)). The same abrupt fracture mechanism occurs when the $qTPC_{60}$ is stretched along the x and y directions. Since the central C_{60} unity in $qTPC_{60}$ is connected only with parallel covalent bonds to its next-neighboring units, the fracture pattern is the same regardless of the crystal direction.

4. Conclusions

In summary, We have carried out fully-atomistic reactive (ReaxFF) MD simulations to investigate the thermodynamic stability and stress resilience of $qHPC_{60}$ and $qTPC_{60}$, which were synthesized very recently [16]. These structures are 2D carbon-based materials composed of closely packed quasi-hexagonal and quasi-tetragonal crystalline phases of C_{60} molecules. Their melting processes were investigated by employing heating ramp simulations, with temperatures varying from 300 K to 10,000 K during one ns. $qHPC_{60}$ and $qTPC_{60}$ maintain their structural integrity up to 3500 K. After this critical value, the thermal vibrations impose substantial changes in their morphologies, and the melting process occurs. We obtained similar melting points of 3898 K and 3965 K for $qHPC_{60}$ and $qTPC_{60}$, respectively. The melting process of these structures occurs differently. For the $qHPC_{60}$, the C_{60} units are fragmented into several linear atomic chains (LACs) at 1600 K. The $qTPC_{60}$ structure, in turn, tends to fragment into separated C_{60} units at 1200 K. For the stress response as a function of the uniaxial applied strain, the first noticeable feature is that $qHPC_{60}$ and $qTPC_{60}$ have a anisotropic mechanical behavior. They are more resilient to tension along the x-direction than along the y-one. The presence of a ring composed of four carbon atoms linking the C_{60} units makes them less resilient to tension along the y-direction. Moreover, these materials present a well-defined (linear) elastic region when subjected to uniaxial tensile loading. $qHPC_{60}$ and $qTPC_{60}$ undergo an abrupt structural transition to a fractured form after a critical strain. $qHPC_{60}$ monolayer breaks abruptly with fast and linear crack propagation when stretched along the x-direction. Conversely, non-linear rapid crack propagation was observed by stretching $qHPC_{60}$ along the y-direction. A similar abrupt fracture mechanism occurs when the $qTPC_{60}$ is stretched along the x and y directions. Since a central C_{60} unity in $qTPC_{60}$ is connected only with parallel covalent bonds to its next-neighboring units, the fracture pattern is the same regardless of the crystal direction.

The following Young's modulus values for $qHPC_{60}$ and $qTPC_{60}$ were estimated: 175.9 GPa (218.5 GPa) for x-direction (y-direction) and 100.7 GPa (133.5 GPa) for x-direction (y-direction), respectively. $qHPC_{60}$ tends to be more resilient than $qTPC_{60}$ due to the higher number of covalent bonds connecting the next-neighboring C_{60} units.

CRediT authorship contribution statement

L.A. Ribeiro Junior: Data curation, Formal analysis, Methodology, Writing – original draft. **M.L. Pereira Junior:** Data curation, Formal analysis, Methodology, Writing – original draft. **W.F. Giozza:** Conceptualization, Supervision, Funding acquisition, Writing – review & editing. **R.M. Tromer:** Data curation, Formal analysis, Methodology, Writing – original draft. **Douglas S. Galvão:** Conceptualization, Supervision, Funding acquisition, Writing – review & editing.

Declaration of competing interest

The authors declare the following financial interests/personal relationships which may be considered as potential competing interests: Luiz A. Ribeiro Junior reports financial support was provided by Foundation for Research Support of the Federal District. Douglas S. Galvao reports financial support was provided by State of Sao Paulo Research Foundation. Raphael M. Tromer reports financial support was provided by State of Sao Paulo Research Foundation. Luiz A. Ribeiro Junior reports financial support was provided by National Council for Scientific and Technological Development.

Data availability

No data was used for the research described in the article.

Acknowledgments

This work was financed by the Coordenação de Aperfeiçoamento de Pessoal de Nível Superior (CAPES), Brazil - Finance Code 001, Conselho Nacional de Desenvolvimento Cientifico e Tecnológico (CNPq), Brazil, FAP-DF, and FAPESP, Brazil. We thank the Center for Computing in Engineering and Sciences at Unicamp for financial support through the FAPESP/CEPID Grants #2013/08293-7 and #2018/11352-7. L.A.R.J acknowledges the financial support from a FAP-DF grants 00193-00000857/2021-14 and 00193-00000811/2021-97, and CNPq, Brazil grants 302922/2021-0 and 350176/2022-1. W.F.G acknowledges the financial support from a FAP-DF grant 00193-00000853/2021-28. L.A.R.J. gratefully acknowledges the support from ABIN grant 08/2019 and Fundação de Apoio à Pesquisa (FUNAPE), Brazil, Edital 02/2022 - Formulário de Inscrição N.4. L.A.R.J. acknowledges Núcleo de Computação de Alto Desempenho (NACAD) and for providing the computational facilities. This work used resources of the Centro Nacional de Processamento de Alto Desempenho em São Paulo (CENAPAD-SP).

References

[1] Kostya S Novoselov, Andre K Geim, Sergei V Morozov, De-eng Jiang, Yanshui Zhang, Sergey V Dubonos, Irina V Grigorieva, Alexandr A Firsov, Electric field effect in atomically thin carbon films, Science 306 (5696) (2004) 666–669.

[2] Rajesh Kumar, Ednan Joanni, Rajesh K Singh, Dinesh P Singh, Stanislav A Moshkalev, Recent advances in the synthesis and modification of carbon-based 2D materials for application in energy conversion and storage, Prog. Energy Combust. Sci. 67 (2018) 115–157.

[3] Haigang Lu, Si-Dian Li, Two-dimensional carbon allotropes from graphene to graphyne, J. Mater. Chem. C 1 (23) (2013) 3677–3680.

[4] Zhanyu Wang, F Dong, Bo Shen, RJ Zhang, YX Zheng, LY Chen, SY Wang, CZ Wang, KM Ho, Yuan-Jia Fan, et al., Electronic and optical properties of novel carbon allotropes, Carbon 101 (2016) 77–85.

[5] Andrey N. Enyashin, Alexander L. Ivanovskii, Graphene allotropes, Phys. Status Solidi (B) 248 (8) (2011) 1879–1883.

[6] Zhenhai Wang, Xiang-Feng Zhou, Xiaoming Zhang, Qiang Zhu, Huafeng Dong, Mingwen Zhao, Artem R Oganov, Phagraphene: a low-energy graphene allotrope composed of 5–6–7 carbon rings with distorted dirac cones, Nano Lett. 15 (9) (2015) 6182–6186.

[7] Shuaiwei Wang, Baocheng Yang, Houyang Chen, Eli Ruckenstein, Popgraphene: a new 2D planar carbon allotrope composed of 5–8–5 carbon rings for high-performance lithium-ion battery anodes from bottom-up programming, J. Mater. Chem. A 6 (16) (2018) 6815–6821.

[8] Zhiwen Zhuo, Xiaojun Wu, Jinlong Yang, Me-graphene: a graphene allotrope with near zero Poisson's ratio, sizeable band gap, and high carrier mobility, Nanoscale 12 (37) (2020) 19359–19366.
[9] Nataliya N. Karaush, Gleb V. Baryshnikov, Boris F. Minaev, DFT characterization of a new possible graphene allotrope, Chem. Phys. Lett. 612 (2014) 229–233.
[10] Run-Sen Zhang, Jin-Wu Jiang, The art of designing carbon allotropes, Front. Phys. 14 (1) (2019) 1–17.
[11] Chee-Tat Toh, Hongji Zhang, Junhao Lin, Alexander S Mayorov, Yun-Peng Wang, Carlo M Orofeo, Darim Badur Ferry, Henrik Andersen, Nurbek Kakenov, Zenglong Guo, et al., Synthesis and properties of free-standing monolayer amorphous carbon, Nature 577 (7789) (2020) 199–203.
[12] Qitang Fan, Linghao Yan, Matthias W Tripp, Ondřej Krejčí, Stavrina Dimosthenous, Stefan R Kachel, Mengyi Chen, Adam S Foster, Ulrich Koert, Peter Liljeroth, et al., Biphenylene network: A nonbenzenoid carbon allotrope, Science 372 (6544) (2021) 852–856.
[13] Savas Berber, Eiji Osawa, David Tománek, Rigid crystalline phases of polymerized fullerenes, Phys. Rev. B 70 (2004) 085417.
[14] Abduljabar Qassem Alsayoud, Venkateswara Rao Manga, Krishna Muralidharan, Joshua Vita, Stefan Bringuier, Keith Runge, Pierre Deymier, Atomistic insights into the effect of polymerization on the thermophysical properties of 2-D C60 molecular solids, Carbon 133 (2018) 267–274.
[15] Rinaldo Raccichini, Alberto Varzi, Stefano Passerini, Bruno Scrosati, The role of graphene for electrochemical energy storage, Nature Mater. 14 (3) (2015) 271–279.
[16] Lingxiang Hou, Xueping Cui, Bo Guan, Shaozhi Wang, Ruian Li, Yunqi Liu, Daoben Zhu, Jian Zheng, Synthesis of a monolayer fullerene network, Nature 606 (7914) (2022) 507–510.
[17] Thomas P Senftle, Sungwook Hong, Md Mahbubul Islam, Sudhir B Kylasa, Yuanxia Zheng, Yun Kyung Shin, Chad Junkermeier, Roman Engel-Herbert, Michael J Janik, Hasan Metin Aktulga, et al., The ReaxFF reactive force-field: development, applications and future directions, Npj Comput. Mater. 2 (1) (2016) 1–14.
[18] Roger Smith, Kenny Jolley, Chris Latham, Malcolm Heggie, Adri van Duin, Diana van Duin, Houzheng Wu, A ReaXFF carbon potential for radiation damage studies, Nucl. Instrum. Methods Phys. Res. B 393 (2017) 49–53.
[19] Steve Plimpton, Fast parallel algorithms for short-range molecular dynamics, J. Comput. Phys. 117 (1995) 1–19.
[20] William G. Hoover, Canonical dynamics: equilibrium phase-space distributions, Phys. Rev. A 31 (3) (1985) 1695.
[21] William Humphrey, Andrew Dalke, Klaus Schulten, VMD: Visual molecular dynamics, J. Mol. Graph. 14 (1) (1996) 33–38.
[22] JH Los, KV Zakharchenko, MI Katsnelson, Annalisa Fasolino, Melting temperature of graphene, Phys. Rev. B 91 (4) (2015) 045415.
[23] Levi C Felix, Raphael M Tromer, Pedro AS Autreto, Luiz A Ribeiro Junior, Douglas S Galvao, On the mechanical properties and thermal stability of a recently synthesized monolayer amorphous carbon, J. Phys. Chem. C 124 (27) (2020) 14855–14860.
[24] ML Pereira, WF da Cunha, RT de Sousa, GD Amvame Nze, DS Galvão, LA Ribeiro, On the mechanical properties and fracture patterns of the nonbenzenoid carbon allotrope (biphenylene network): a reactive molecular dynamics study, Nanoscale 14 (8) (2022) 3200–3211.